energies

MDPI

Article

Magnetic Saturation Parameter Identification of Hybrid Excitation Generator Based on Particle Swarm Optimization

Rui Jing, Xinqiang Yi, Yapeng Jiang, Zhifang Yuan * and Wenzhong Yu

National Key Laboratory of Electromagnetic Energy, Naval University of Engineering, Wuhan 430033, China; m25180801@nue.edu.cn (R.J.)

* Correspondence: yuanzhifang23@nue.edu.cn

Abstract

Hybrid excitation generators offer high power density and adjustable magnetic field, making them attractive for power generation applications with strict volume and weight constraints. However, under strong field excitation conditions, deep saturation of the iron core leads to a strongly nonlinear relationship between the resultant air-gap flux linkage and the field current, causing traditional linear models to exhibit large errors in the saturation region. To address this issue, this paper proposes a piecewise nonlinear function-based method for fitting magnetic saturation characteristics. The function's nonlinear trend is exploited to construct an analytical model that describes the flux–current relationship in both the linear and deep saturation regions. The unknown model parameters are then determined by solving an optimization problem that minimizes the sum of squared output voltage errors. Particle swarm optimization (PSO) is employed for global search, overcoming the challenges of initial-value dependence and local optima in such multimodal parameter spaces. Experimental data from a hybrid excitation generator are used as samples for validation. The results show that the nonlinear model optimized by PSO accurately fits the flux linkage variation over the full current range, reducing the error from 7.78% to approximately 1%. The proposed model is concise in form, requires low computational effort, and can be directly used as an accurate analytical method for performance analysis of hybrid excitation generators, demonstrating good engineering application value.

Keywords: hybrid excitation generator; magnetic saturation; nonlinear fitting; particle swarm optimization; parameter identification

1. Introduction

1.1. General Overview

A hybrid excitation generator (HEG) combines the high power density and high efficiency of permanent magnet machines with the flexible air-gap flux adjustability of electrically excited machines, making it highly promising for applications such as aircraft power supplies and marine propulsion [1]. However, under heavy load or strong field excitation conditions, the stator and rotor core materials enter the saturation region, resulting in a nonlinear coupling relationship between the resultant air-gap flux linkage and the field winding current. Traditional linear-model-based approaches suffer from dramatically increased errors in the saturation region, which severely restricts accurate electromagnetic performance analysis of the generator [2].

Academic Editor: Krzysztof Górecki

Received: 15 June 2026

Revised: 30 July 2026

Accepted: 8 September 2026

Published: 16 September 2026

1.2. Literature Review and Motivation

Various methods have been proposed by researchers to address the modeling of magnetically saturated nonlinear generators. In ref. [3], finite element simulation is employed to finely capture the nonlinear magnetization and complex geometry of the iron core, achieving high accuracy. In ref. [4], a nonlinear model of the field winding inductance is developed, and its accuracy is verified through finite element analysis (FEA) and experiments. Reference [5] analyzed the geometric structure and efficiency curve of permanent magnet synchronous motors through finite element and analytical methods, accurately analyzed the model and verified it. In ref. [6], a three-dimensional finite element model is combined with a three-dimensional magnetic equivalent circuit (MEC) model, achieving a trade-off between generality and computational speed to some extent. In refs. [7–10], the magnetic equivalent circuit method is applied to analyze permanent magnet synchronous generator or hybrid excitation generators, achieving a trade-off between speed and accuracy to some extent. In ref. [11], an analytical method (AM) is adopted to investigate inductance imbalance and saturation effects, where a sigmoid function is introduced to describe the no-load flux linkage and back electromotive force generated during segmented movement of the mover, thereby accurately simulating various generator effects. In summary, although existing methods offer high accuracy in finite element analysis and fast computation in magnetic equivalent circuit methods, they still suffer from the drawbacks of long computational time [12] in the former and limited accuracy in the latter. Achieving a balance among saturation-region accuracy, analytical conciseness, and computational efficiency remains challenging. A modeling approach that can accurately describe the complete flux linkage characteristics from the linear region to the deep saturation region while being convenient for engineering applications is still lacking. In ref. [13], nonlinear magnetization and local saturation effects in the pole region are considered, and a saturation factor is introduced to modify the linear model. Table 1 summarizes various methods for solving the modeling problem of magnetic saturation nonlinear generators as well as their advantages and disadvantages. Parameters are extracted with the aid of finite element analysis to improve accuracy, but the extraction process remains slow. Therefore, a parameter identification method with both high accuracy and faster extraction speed is needed.

Table 1. Current Status of Methods for Magnetic Saturation Nonlinearity.

References	Methods	Advantages and Disadvantages
[3] [4] [5] [6]	FEA FEA FEA + AM FEA + MEC	High accuracy, but low computational speed
[7] [8] [9] [10]	EMN EMN EMN EMN	Improved computational speed but limited accuracy
[11]	AM	High accuracy and speed, but different applicable scopes
[13]	EMN + AM + FEA	High accuracy and computational speed, but parameter extraction is slow

Particle swarm optimization (PSO) has been widely applied in the field of motor parameter identification due to its simplicity, fast convergence, and global search capability [14–16]. According to the existing literature, PSO-based parameter identification methods are mostly applied to permanent magnet synchronous generators (PMSMs). In ref. [17], a dynamic self-learning PSO (DSLPSO) method is proposed to globally identify electrical parameters, mechanical parameters, and inverter nonlinearities as a whole. In ref. [18], PSO is combined with chaos theory to optimize the design parameters of a permanent magnet synchronous generator for improved power density. To address the high computational cost of PSO-based identification, a fast PSO algorithm is proposed in [19] to achieve rapid and high-precision identification of d- and q-axis inductances and permanent magnet flux linkage. In ref. [20], an improved chaotic PSO (ICPSO) algorithm is developed by integrating chaos, PSO, and elite immune principles, and its effectiveness is validated experimentally. In ref. [21], an online PSO method is proposed to identify parameters of a surface-mounted permanent magnet synchronous generator, determining key parameters such as flux linkage and inductance. In ref. [22], a niche chaotic PSO (NCOPSO) algorithm is proposed, which enhances global search capability by constructing niche populations and applying chaotic mutation to the optimal particle, enabling simultaneous identification of four parameters—stator resistance, d- and q-axis inductances, and permanent magnet flux linkage—with effectively reduced identification errors. Relatively few studies have applied PSO to parameter identification of induction generators or Induction Motors. For example, in ref. [23], an improved PSO algorithm with dynamic inertia weight is proposed, where the influence of saturation effects is considered in the parameter identification process of an induction motor (IM), and its effectiveness is verified through algorithm comparison. In ref. [24], PSO is combined with reinforcement learning to identify parameters of a doubly fed induction generator (DFIG), significantly reducing the identification error. Table 2 summarizes the applications of PSO or improved PSO algorithms on different generator models.

Table 2. PSO for Parameter Identification in Electric Machines.

References	Application Object	Methods
[17]	PMSM	DSLPSO
[18]	PMSM	PSO + chaos theory
[19]	PMSM	Fast PSO
[20]	PMSM	ICPSO
[21]	SPMSM	Online PSO
[22]	PMSM	NCOPSO
[23]	IM	Improved PSO
[24]	DFIG	PSO + RL

In summary, no prior work has been found in the literature that applies PSO to the analysis of magnetic saturation effects in hybrid excitation synchronous generators. Under the strong excitation condition of the hybrid excitation generator, the deep saturation of the core leads to a nonlinear relationship between the syngas gap flux link-age and the excitation current. Traditional linear models have large errors in the saturation region or lack rapid simulation methods. Therefore, in-depth research will be conducted on the application of PSO in the field of magnetic saturation effect analysis of hybrid excitation generators.

1.3. Paper Structure

To address the above issues, this paper proposes a PSO-based parameter identification method for magnetic saturation nonlinearity in hybrid excitation generators. First, at the model structure level, a piecewise nonlinear fitting function is adopted as the basic description form of the flux linkage. This function captures the physical law that the resultant air-gap flux linkage asymptotically saturates as the current increases, and exhibits favorable mathematical properties—smoothness, monotonicity, and boundedness—over the full current range. Second, at the parameter identification level, the determination of the unknown parameters of the fitting function is formulated as an optimization problem that minimizes the sum of squared output voltage errors. The particle swarm optimization (PSO) algorithm is employed to solve this problem, leveraging its advantages of simplicity, fast convergence, and global search capability, thereby overcoming the difficulties of initial-value dependence and susceptibility to local optima in such multimodal parameter spaces. Finally, the parameters optimized by PSO are substituted into the nonlinear fitting function. The effectiveness and accuracy of the proposed method are validated through comparison between simulation results and experimental data, demonstrating its good engineering practical value.

2. Nonlinear Modeling of Magnetic Saturation in Hybrid Excitation Generators

2.1. Saturation Characteristic Analysis and Modeling Requirements

The core of a hybrid excitation generator is made of soft magnetic materials such as silicon steel sheets. Its B-H curve, shown in Figure 1, exhibits typical nonlinear characteristics: the flux density increases approximately linearly in the low magnetic field strength region; as the field strength increases, the permeability gradually decreases, and the flux density growth slows down after the material enters the saturation region.

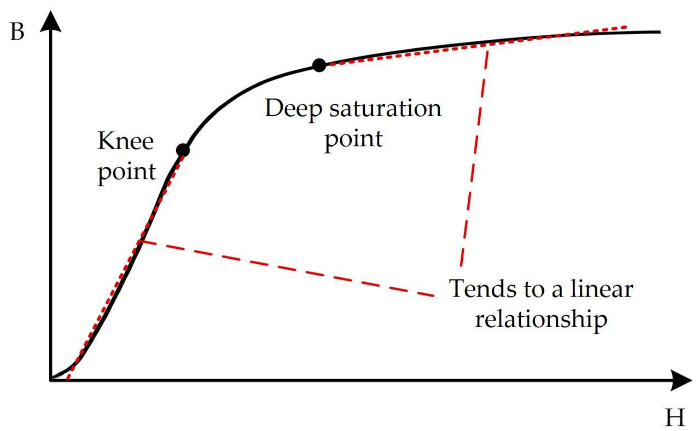

Figure 1. B-H curve.

The uniqueness of the hybrid excitation generator lies in the fact that the magnetic field is established jointly by the permanent magnets and the field winding, and the operating point of the magnetic circuit is affected by both the field current and the armature current. The magnetomotive forces generated by the two sources superimpose, causing the core saturation level to vary dynamically with operating conditions, resulting in a strongly nonlinear coupling relationship between flux linkage and current.

The above saturation nonlinearity is directly reflected in the flux linkage–current characteristics. In the low-current region, the flux linkage increases approximately linearly. As the current increases, the growth rate of the flux linkage gradually slows down, and the increment becomes extremely limited in the deep saturation region. Under different combinations of field current and armature current, both the saturation knee point and the asymptotic value of the curve family shift. This characteristic makes traditional linear models with fixed slopes produce significant errors in the saturation region, while piecewise linearization or simple polynomial fitting fails to provide a smooth and continuous description over the entire operating range. Therefore, an explicit nonlinear model that can uniformly describe the complete flux linkage characteristics from the linear region to the deep saturation region, and is concise in form, is required.

2.2. HEG System and Basic Equations

The block diagram of the HEG system is shown in Figure 2, and the topology diagram of the twelve-phase hybrid excitation generator is shown in Figure 3.

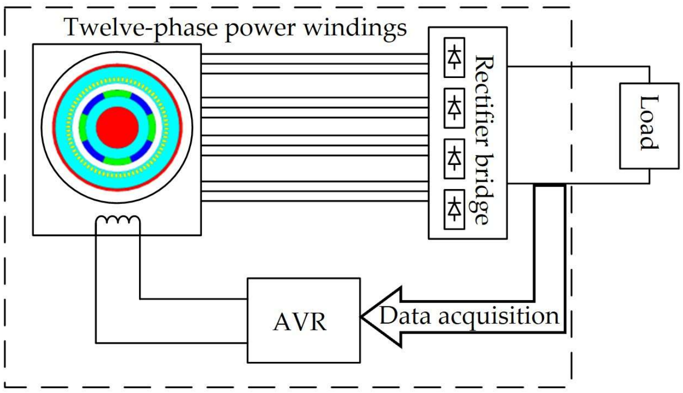

Figure 2. Block diagram of HEG system.

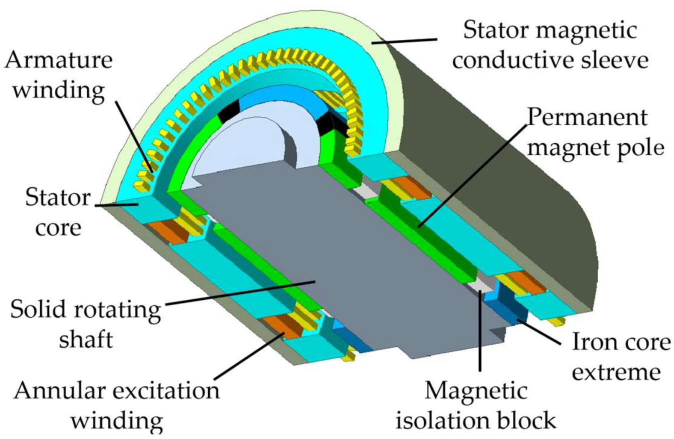

Figure 3. Hybrid excitation generator topology diagram.

Among them, an AVR (Automatic Voltage Regulator) is an automatic excitation control device that maintains the terminal voltage of a synchronous generator at a prescribed level by regulating the field current in response to grid disturbances or load variations. The hybrid excitation generator model is established in the d-q rotating coordinate system, and the flux linkage equations and voltage equations of the generator can be expressed as Equations (1) and (2), respectively:

$$\boldsymbol{\psi}_{\mathrm{dq}} = \boldsymbol{\psi}_{\mathrm{pmd}} + \boldsymbol{L}_{\mathrm{dq}}\boldsymbol{i}_{\mathbf{dq}}, \tag{1}$$

$$\boldsymbol{u}_{\mathrm{dq}} = \frac{\mathrm{d}\boldsymbol{\psi}_{\mathrm{dq}}}{\mathrm{dt}} + \omega_{\mathrm{s}}\boldsymbol{G}\boldsymbol{\psi}_{\mathrm{dq}} - \boldsymbol{R}_{\mathrm{dq}}\boldsymbol{i}_{\mathbf{dq}}, \tag{2}$$

where $\boldsymbol{\psi}_{\mathrm{dq}}$ is the stator and rotor flux linkage column vector; $\boldsymbol{u}_{\mathrm{dq}}$ is the stator and rotor voltage column vector; $\boldsymbol{i}_{\mathrm{dq}}$ is the stator and rotor current column vector; $\boldsymbol{R}_{\mathrm{dq}}$ is the stator and rotor resistance matrix; ω_{s} is the electrical angular speed of the generator; $\boldsymbol{L}_{\mathrm{dq}}$ is the stator and rotor inductance matrix; and $\boldsymbol{G}$ is the sign matrix [25].

$\boldsymbol{\psi}_{\mathrm{pmd}}$ = $[\psi_{\mathrm{pmd0}}\ 0\ \psi_{\mathrm{pmd0}}\ 0\ \psi_{\mathrm{pmd0}}\ 0\ \psi_{\mathrm{pmd0}}\ 0\ \psi_{\mathrm{pmd0}}\ 0\ \psi_{\mathrm{pmd0}}\ 0]^{\mathrm{T}}$ is the remanent flux linkage column vector; ψ_{pmd0} is the amplitude of the permanent magnet flux linkage, which can be obtained by setting $\boldsymbol{i}_{\mathrm{dq}}$ to zero. This paper focuses on the nonlinear fitting of the flux linkage equation, and ψ_{pmd0} is assumed to be a known quantity.

https://doi.org/10.3390/en19184390

2.3. Construction of Nonlinear Fitting Function for Magnetic Saturation

The generator modeling method proposed in this paper mainly considers the influence of the field current of the electrically excited part on the field winding inductance, which in turn affects the overall generator performance. However, to establish a complete model, the stator and rotor inductance matrix $\boldsymbol{L}_{\mathrm{dq}}$ is processed nonlinearly using a piecewise fitting function to accurately characterize the inductance characteristics of the generator under different saturation levels. Meanwhile, the literature and monograph [26,27] provide references for the identification of inductance parameters of the excitation winding and armature winding in this paper, and the monograph [28] offers references for the measurement methods of other parameters in this paper.

To this end, as shown in Equation (3), the d-q axis resultant air-gap flux linkage ψ_{m} is introduced as the criterion for determining the core saturation level, providing a quantitative benchmark for the subsequent nonlinear correction of the stator and rotor inductance matrix L_{dq}.

$$\psi_{\mathrm{m}} = \sqrt{\psi_{\mathrm{dm}}^2 + \psi_{\mathrm{qm}}^2}, \tag{3}$$

where $\psi_{\mathrm{dm}} = L_{\mathrm{ad}}(-i_{\mathrm{d1}} - i_{\mathrm{d2}} - i_{\mathrm{d3}} - i_{\mathrm{d4}} - i_{\mathrm{fd}} - i_{\mathrm{kd}})$ and $\psi_{\mathrm{qm}} = L_{\mathrm{aq}}(-i_{\mathrm{q1}} - i_{\mathrm{q2}} - i_{\mathrm{q3}} - i_{\mathrm{q4}} - i_{\mathrm{fq}} - i_{\mathrm{kq}})$. ψ_{dm} and ψ_{qm} are the d-axis and q-axis air-gap flux linkages, respectively. i_{d1}, i_{d2}, i_{d3}, and i_{d4} are the currents of the four d-axis stator armature windings, and i_{q1}, i_{q2}, i_{q3}, and i_{q4} are the currents of the four q-axis stator armature windings. The armature reaction generated by these currents exhibits a demagnetizing effect. The d- and q-axis field winding currents i_{fd} and i_{fq} constitute the magnetizing currents. i_{kd} and i_{kq} are the d-axis and q-axis damper winding currents.

To achieve nonlinearization of the stator and rotor inductance matrix L_{dq}, the proposed generator modeling method introduces a saturation correction coefficient K_{m}. The d- and q-axis stator armature reaction inductances L_{ad} and L_{aq}, which enter the saturation state, are then corrected using Equations (4) and (5), respectively:

$$L_{\mathrm{ad}} = \begin{cases} L_{\mathrm{ad0}} & ,\psi_{\mathrm{m}} \le \psi_{\mathrm{m1}} \\ \frac{(\psi_{\mathrm{m1}} + (\psi_{\mathrm{m}} - \psi_{\mathrm{m1}})K_{\mathrm{m}})\psi_{\mathrm{dm}}}{\psi_{\mathrm{m}}(-i_{\mathrm{d1}} - i_{\mathrm{d2}} - i_{\mathrm{d3}} - i_{\mathrm{d4}} + i_{\mathrm{fd}} + i_{\mathrm{kd}})} & ,\psi_{\mathrm{m}} > \psi_{\mathrm{m1}} \end{cases}, \tag{4}$$

$$L_{\mathrm{aq}} = \begin{cases} L_{\mathrm{aq0}} & ,\psi_{\mathrm{m}} \le \psi_{\mathrm{m1}} \\ \frac{(\psi_{\mathrm{m1}} + (\psi_{\mathrm{m}} - \psi_{\mathrm{m1}})K_{\mathrm{m}})\psi_{\mathrm{dm}}}{\psi_{\mathrm{m}}(-i_{\mathrm{q1}} - i_{\mathrm{q2}} - i_{\mathrm{q3}} - i_{\mathrm{q4}} + i_{\mathrm{fq}} + i_{\mathrm{kq}})} & ,\psi_{\mathrm{m}} > \psi_{\mathrm{m1}} \end{cases}, \tag{5}$$

where L_{ad0} and L_{aq0} are the initial unsaturated d- and q-axis stator armature reaction inductances. As shown in Equation (6), when the equivalent d-q axis flux linkage ψ_{m} exceeds the knee-point flux linkage threshold ψ_{m1}, the generator is determined to be in the saturation state. The specific expression of the saturation correction coefficient K_{m} is as follows. K_{m} is a real number between 0 and 1, with a lower limit K_{m1} set to approximate the extreme saturation state of the generator. Meanwhile, a quadratic-fitting nonlinear operating region—i.e., the transition region between the unsaturated and deeply saturated states—is defined, where $\psi_{\mathrm{m1}} < \psi_{\mathrm{m}} \le \psi_{\mathrm{m2}}$.

$$K_{\mathrm{m}} = \begin{cases} 1 & ,\psi_{\mathrm{m}} \le \psi_{\mathrm{m1}} \\ 1 - (1 - K_{\mathrm{m1}})\left(1 - e^{-3\frac{(\psi_{\mathrm{m}} - \psi_{\mathrm{m1}})}{(\psi_{\mathrm{m2}} - \psi_{\mathrm{m1}})}}\right) & ,\psi_{\mathrm{m1}} < \psi_{\mathrm{m}} \le \psi_{\mathrm{m2}} \\ K_{\mathrm{m1}} & ,\psi_{\mathrm{m}} > \psi_{\mathrm{m2}} \end{cases}, \tag{6}$$

In the quadratic-fitting nonlinear operating region, starting from the onset of saturation, the saturation correction coefficient K_{m} gradually decreases from 1 as ψ_{m} increases; a smaller coefficient value indicates a deeper saturation level of the generator core. When the equivalent d-q axis flux linkage ψ_{m} exceeds the deep saturation point threshold (the upper limit of the nonlinear operating region) ψ_{m2}, the saturation correction coefficient K_{m} remains constant at its lower limit K_{m1}.

Taking advantage of the symmetrical characteristic of bidirectional excitation in the hybrid excitation generator, the same flux linkage fitting function form is shared for both positive and negative excitation, thereby simplifying the establishment of the saturation model. Only the identification of different parameter points under forward and reverse excitation is required.

The characteristic curve of ferromagnetic materials is shown in Figure 1. Typically, before the knee point, the B-H relationship can be considered linear. Between the knee point and the saturation point, as the excitation current continues to increase, the output voltage rise rate of the generator slows down significantly, exhibiting nonlinear characteristics. After reaching the deep saturation point, the growth rate becomes extremely slow and can be approximated as a linear increase with a very small slope. The parameters to be identified are listed in Table 3, where (I) and (II) denote positive and negative excitation currents, respectively.

Table 3. Parameters to be identified.

Symbol	Parameter Meaning
ψ_{max1}	Knee-point flux linkage threshold (I)
ψ_{mf1}	Deep saturation point flux linkage threshold (I)
K_{m1}	Lower limit of saturation correction coefficient (I)
ψ_{max2}	Knee-point flux linkage threshold (II)
ψ_{mf2}	Deep saturation point flux linkage threshold (II)
K_{m2}	Lower limit of saturation correction coefficient (II)

In summary, by incorporating the saturation correction coefficient K_{m}, which takes different values in different operating stages, into the nonlinear stator and rotor inductance matrix L_{dq}, a nonlinear description of the generator is achieved.

3. Parameter Identification Method Based on Particle Swarm Optimization

3.1. Principle of Standard Particle Swarm Optimization

PSO is a swarm intelligence algorithm proposed by psychologist J. Kennedy and computer scientist R. Eberhart [29]. Inspired by the foraging behavior of bird flocks, PSO takes advantage of information exchange among individuals within a population to achieve iterative optimization through continuous competition and cooperation. A schematic diagram of its principle is shown in Figure 4.

In the PSO algorithm, each particle contains only its own velocity and position information. During each iteration, the algorithm updates the individual information of particles according to the velocity and position update rules. The position and velocity update formulas are given in Equations (7) and (8), respectively.

$$x_i(t+1) = x_i(t) + v_i(t+1), \tag{7}$$

$$v_i(t+1) = w \cdot v_i(t) + c_1 \cdot \mathrm{rand}_1 \cdot (pBest_i - x_i(t)) + c_2 \cdot \mathrm{rand}_2 \cdot (gBest - x_i(t)), \tag{8}$$

where x_i(t) and x_i(t + 1) are the positions of particle i at times t and t + 1, respectively; v_i(t) and v_i(t + 1) are the velocities of particle i at times t and t + 1, respectively; w is the inertia weight; c_1 and c_2 are the cognitive coefficient and social coefficient; rand_1 and rand_2 are random numbers uniformly distributed in [0, 1]; and $pBest_i$ and $gBest$ are the individual best position and the global best position of particle i, respectively.

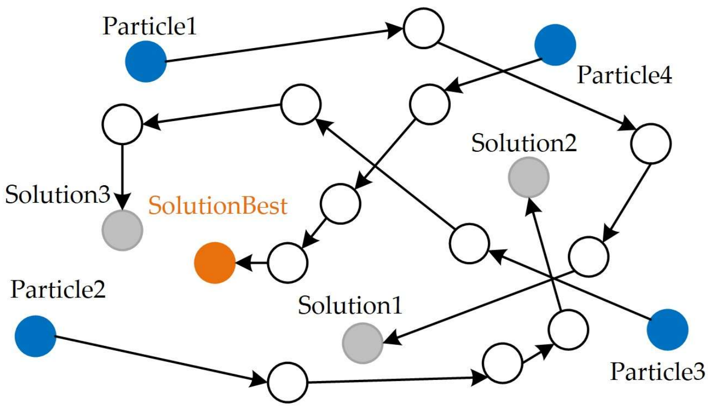

Figure 4. Schematic Diagram of PSO Principle.

3.2. Design of PSO Parameter Identification Strategy

The fitness function in this paper is defined in Equation (9) as the sum of squared differences between the simulated output DC voltage U_{dc_s} and the experimental output DC voltage U_{dc_t}, where n is the number of output values.

$$f(n) = \sum_1^n (U_{dc\_s} - U_{dc\_t})^2, \tag{9}$$

The parameter settings of the PSO algorithm are listed in Table 4. The dimension dim is the number of parameters to be identified. The population size, n_{Pop}, and the maximum number of iterations, maxIt, determine the computational complexity and search depth of the algorithm. In this paper, the ratio of n_{Pop} to maxIt is set to 1:5 to ensure a certain search depth while minimizing computational complexity. The inertia weight w controls the extent to which a particle retains its previous velocity. To avoid degraded global search capability due to an excessively low value or oscillation and non-convergence due to an excessively high value, a standard PSO structure with linearly decreasing inertia weight is adopted. The value of w decreases linearly from 0.9 to 0.2 during the iteration process [30]. In the standard PSO algorithm, to ensure convergence, the condition $c_1 + c_2 < 3$ must be satisfied to balance the cognitive and social components. The learning factors are typically set to $c_1 = c_2 = 1.5$. The maximum search velocity and the upper and lower bounds of the parameters to be identified are determined by estimation.

Table 4. PSO parameter settings.

Symbol	Parameter Meaning	Numerical Value
dim	Dimension	20
n_{Pop}	Population Size	4
maxIt	Maximum Number of Iterations	20
w_{ini}	Initial Inertia Weight	0.9
w_{end}	Final Inertia Weight	0.2
c_1	Cognitive Coefficient	1.5
c_2	Social Coefficient	1.5
v_{max}	Maximum Search Velocity	[0.005, 0.005, 0.01, 0.005, 0.005, 0.01]
lb	Lower Bound of Parameters	[0.01, 0.01, 0, 0.01, 0.01, 0]
ub	Upper Bound of Parameters	[0.0713, 0.0713, 1, 0.0713, 0.0713, 1]

Figure 5 shows the flowchart of the algorithm. According to the model definition, the knee-point flux of the magnetization curve must be smaller than the deep saturation point flux; otherwise, the piecewise function loses its physical meaning. Therefore, after each particle position update, the following custom constraint is enforced:

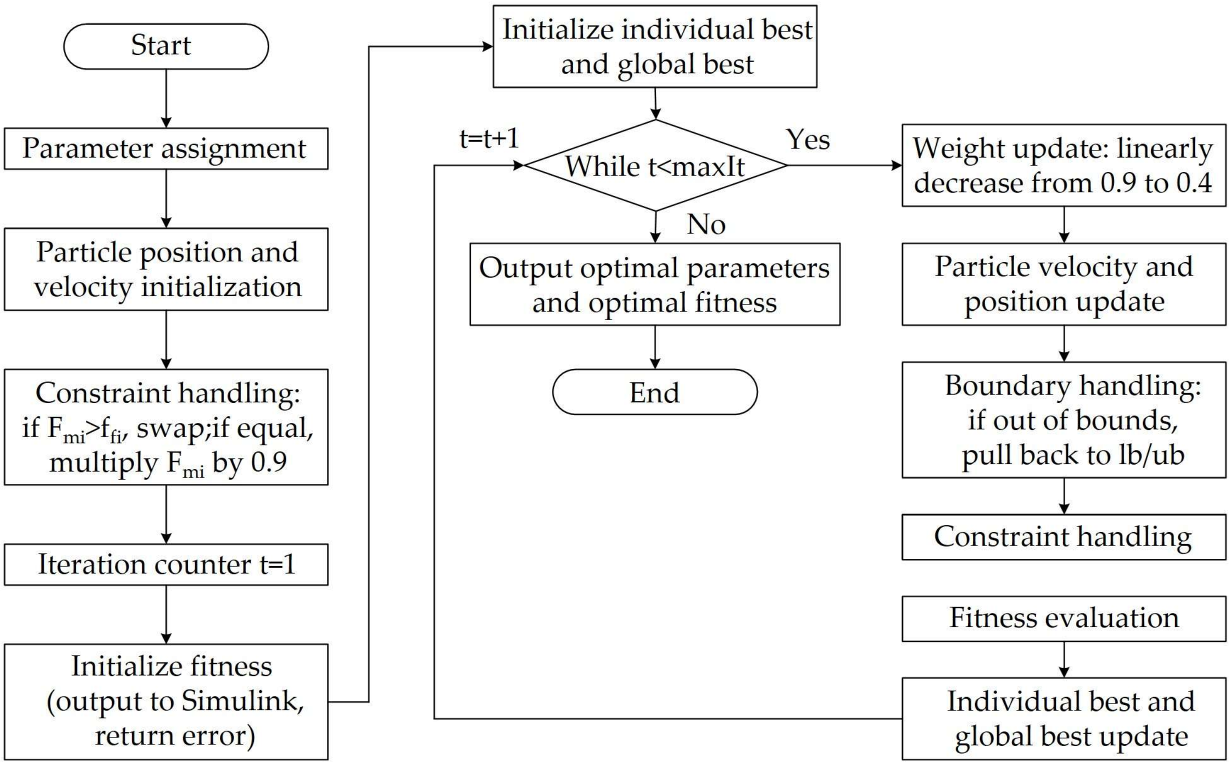

Figure 5. Algorithm flowchart.

If the knee-point flux (F_{mi}) is greater than or equal to the deep saturation point flux (f_{fi}), the two parameter values are swapped. If the two parameters remain equal after swapping, the former parameter is multiplied by 0.9 to strictly enforce the inequality. This constraint introduces no additional distortion to the objective function, ensures free particle movement within the feasible space, and improves both the search efficiency and the reliability of the results for this specific identification problem.

4. Simulation Results and Analysis

In this paper, a per-unit system is adopted for analysis. The rated capacity of the system is selected as the power base, and the rated voltage as the voltage base. The base current and base impedance are derived from the fundamental relationships of the per-unit system.

4.1. PSO Parameter Identification Simulation Model

The parameters obtained through the algorithm flow shown in Figure 3 are substituted into the nonlinear simulation model to construct the PSO-based parameter identification simulation model for the HEG, as shown in Figure 6.

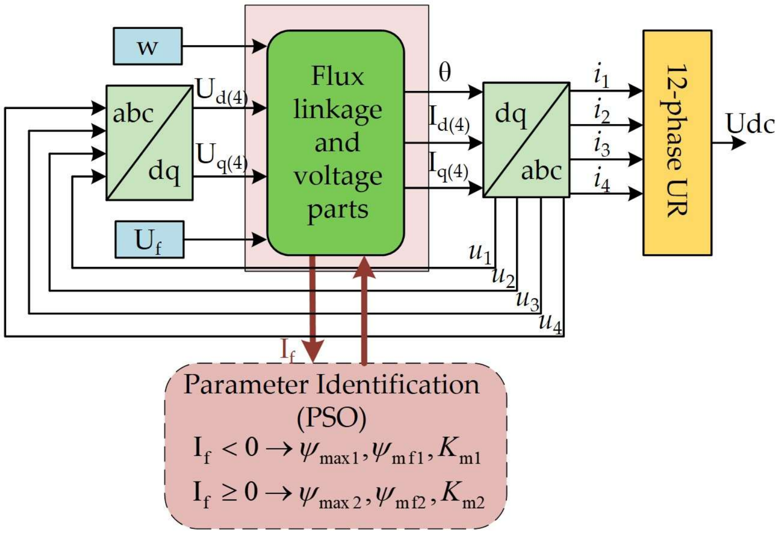

Figure 6. HEG parameter identification model.

4.2. Parameter Identification Convergence Process and Results

As shown in Figure 7, with an increasing number of iterations, the global best fitness gradually decreases and converges, i.e., the error decreases progressively. Considering the randomness of the PSO algorithm, it is difficult to obtain completely consistent single-point convergence results through multiple independent optimizations. Through multiple optimizations, it is found that it converges to a similar interval, approximately within the range of 2.4×10^{-4} to 5×10^{-4}, but most are close to the lower bound. Therefore, in this paper, a compromise is considered to select the result with the optimal fit of 2.8×10^{-4}. The convergence time required for twenty iterations is approximately 5 h, whereas the time required for parameter extraction using a three-dimensional finite element model is several days. Under the premise of satisfying basic error requirements, the particle swarm optimization algorithm significantly reduces the parameter identification time.

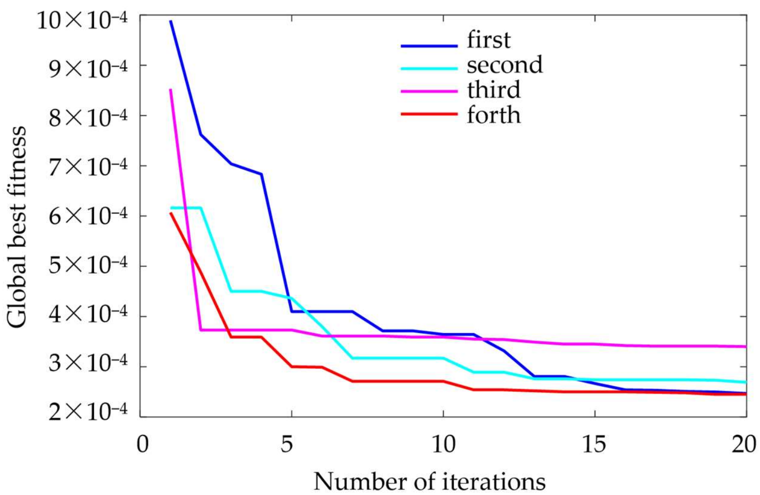

Figure 7. Particle swarm convergence curves.

The parameters identified by the particle swarm optimization algorithm are listed in Table 5.

Table 5. Optimal parameter identification result.

Symbol	PSO Algorithm Identification Results/pu
ψ_{max1}	0.041312
ψ_{mf1}	0.048077
K_{m1}	0.567337
ψ_{max2}	0.043396
ψ_{mf2}	0.059044
K_{m2}	0.417033

4.3. Fitting Accuracy Comparison and Verification

To verify the correctness of the numerical simulation model described above, the simulation results without considering saturation, the simulation results with saturation considered, and the prototype test results are compared.

By analyzing the data in Table 6, it can be seen that after substituting the parameters identified in Table 5 into the nonlinear fitting function proposed in this paper, the maximum relative error of the simulation results is reduced from 7.78% to 1.04% compared with the original model that does not consider saturation. The relative error of the simulation results with saturation considered is generally controlled within 1%, showing good agreement with the experimental no-load characteristics of the generator, except for a slightly higher error of 1.04% at a field current of −0.42 pu. It is worth noting that when the field current is in the range of −0.92 pu to 0.83 pu, the simulation errors of the two models are relatively close. The reason is that within this interval, the generator core has not yet entered the saturation region, and the magnetic circuit operates in the linear region, where the influence of saturation on the flux linkage is negligible. Consequently, both models approximate a linear relationship, and the calculated results naturally tend to be consistent.

Table 6. Simulation and test comparison of no-load characteristics.

Field Current/pu	Original Model Simulation Result/pu	PSO Identification Simulation Result/pu	DC Voltage Test Result/pu	Original Model Simulation Error/%	PSO Identification Simulation Error/%
−1.58	0.800	0.868	0.868	−7.78%	0.05%
−1.42	0.833	0.883	0.880	−5.30%	0.34%
−1.25	0.866	0.897	0.894	−3.13%	0.24%
−1.08	0.899	0.908	0.914	−1.64%	−0.68%
−0.92	0.933	0.933	0.937	−0.44%	−0.44%
−0.75	0.966	0.966	0.963	0.24%	0.24%
−0.58	0.999	0.999	0.994	0.42%	0.42%
−0.42	1.032	1.032	1.021	1.04%	1.04%
−0.25	1.065	1.065	1.060	0.45%	0.45%
0.08	1.098	1.098	1.094	0.31%	0.31%
0.00	1.114	1.114	1.114	0.00%	0.00%
0.17	1.147	1.147	1.149	−0.13%	−0.13%
0.33	1.181	1.181	1.182	−0.14%	−0.15%
0.50	1.214	1.214	1.218	−0.35%	−0.35%
0.67	1.247	1.247	1.248	−0.09%	−0.09%
0.83	1.280	1.280	1.276	0.32%	0.32%
1.00	1.313	1.307	1.308	0.38%	−0.05%
1.17	1.346	1.326	1.328	1.36%	−0.17%
1.33	1.379	1.345	1.344	2.56%	0.04%
1.50	1.412	1.352	1.352	4.42%	0.00%

As shown in Figure 8, by comparing the original model without saturation, the saturation-aware model with parameters optimized by PSO, and the measured no-load characteristic curve, it can be clearly observed that the simulation results of the saturation-aware model are in better agreement with the experimental data, while the original model shows larger deviations. This comparison fully validates the effectiveness and accuracy of the proposed saturation-aware nonlinear model under no-load conditions.

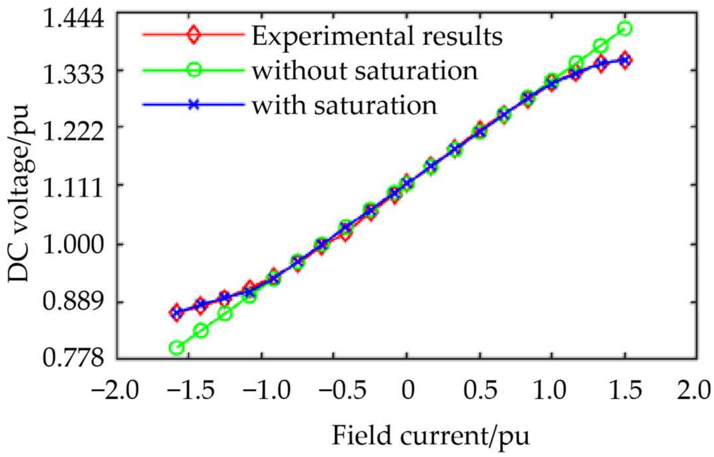

Figure 8. Comparison results of no-load characteristic simulation and tests.

After the no-load characteristic comparison test, to further validate the model accuracy, simulations under various load conditions—with and without saturation effects—are compared, as presented in Table 7. Under rated load, the output voltage from the simulation without saturation is higher than that with saturation, resulting in a larger deviation from the rated voltage. The flux linkage waveforms of the two models under this condition are shown in Figure 9b. Since the machine is only at the initial stage of saturation at this point, the difference between the two flux linkages is relatively small, and consequently the output-voltage deviation remains modest. However, as the saturation level deepens—as illustrated in Figure 9c at 110% load—the system enters the forced-excitation region, where saturation becomes more severe, and the discrepancy between the two models gradually increases. In contrast, for the case depicted in Figure 9a, the load is light and the degree of saturation is low, not yet reaching the deep-saturation stage; therefore, the saturation constraint exerts a negligible influence on this operating condition.

Table 7. Simulation comparison of rated working conditions with and without considering saturation.

Simulation Result	Output Voltage/pu
Without Saturation	1.007
With Saturation	1.003

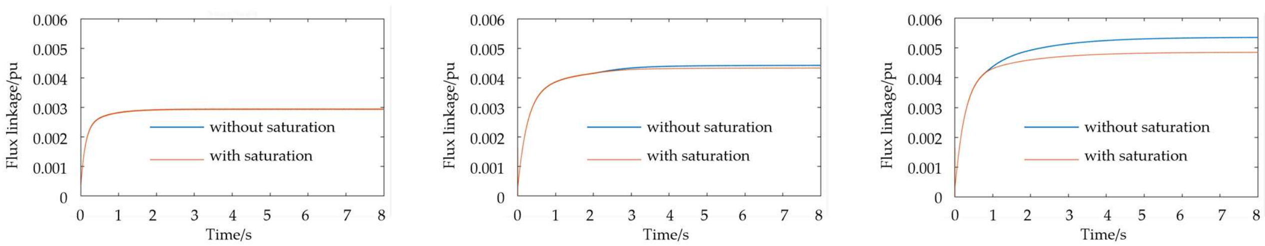

(**a**) 90% load (**b**) 100% load (Rated load) (**c**) 110% load

Figure 9. Flux linkage comparison curves under different load conditions.

After analyzing the steady-state working conditions, the dynamic working condition analysis is carried out. The simulation and test results of the sudden loading and unloading load are shown in Figure 10. Since only the sudden loading and unloading load within the normal working range is conducted in the actual working conditions, only the situation where the sudden loading and unloading load is within the rated load is studied. Its saturation degree is similar to that in Figure 9a and is not subject to saturation constraints. Therefore, the waveform results considered here are consistent with those without saturation, and simulation and experimental comparisons are directly conducted. As shown in the results of Table 8, the simulation is in high agreement with the results. Only when the load is suddenly unloaded, the simulation recovery time is faster than the test time. It is preliminarily analyzed that the identification accuracy of damping parameters is insufficient. Further related research will be carried out in the future.

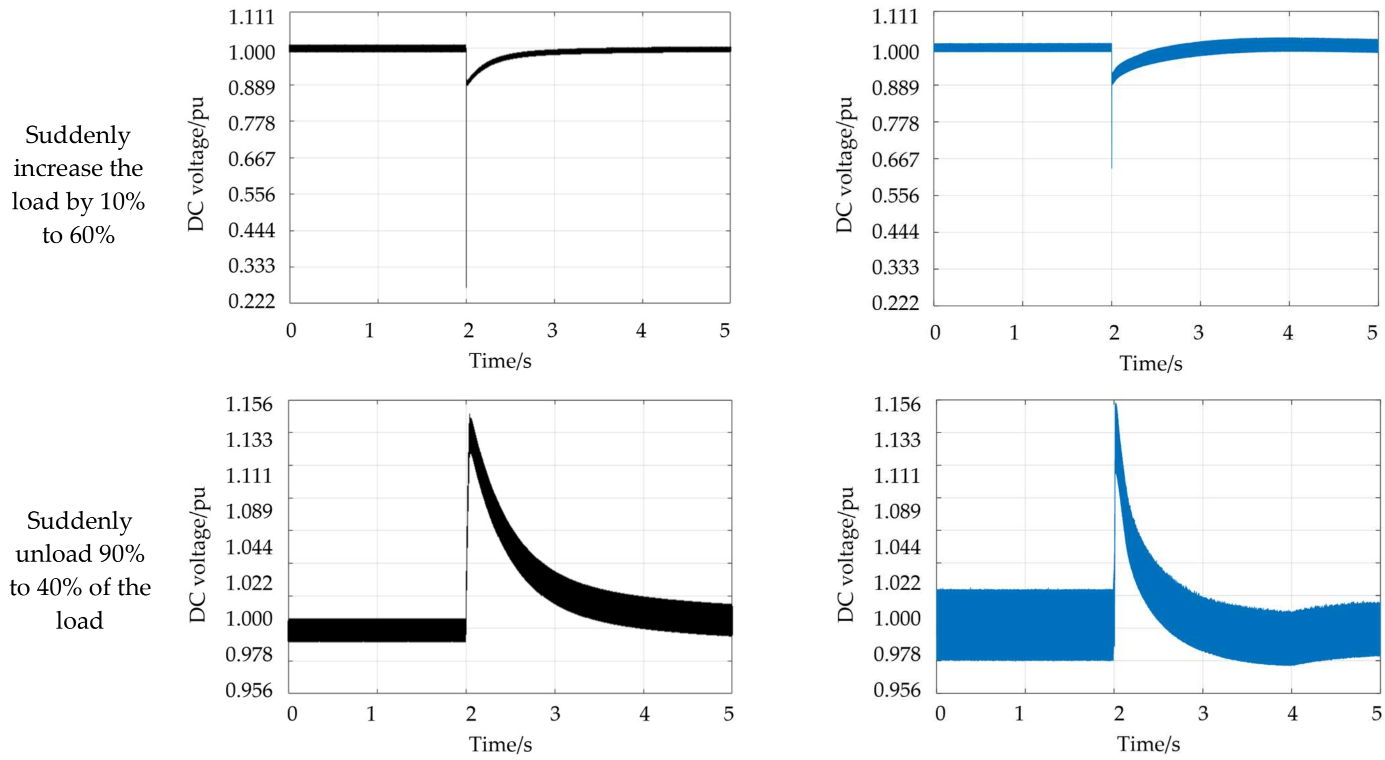

(**a**) Simulation (**b**) Experiment

Figure 10. Comparison of sudden loading and unloading load simulation tests.

Table 8. Comparison of sudden loading and unloading load simulation tests.

Working Condition	Simulation Results of Transient Voltage Change Rate/%	Recovery Time Simulation Results/s	Test Results of the Rate of Change of Transient Voltage/%	Recovery Time Test Results/s
Suddenly increase the load by 10% to 60%	10.78%	0.44	10.33%	0.43
Suddenly unload 90% to 40% of the load	14.12%	0.35	15.23%	0.45

Through the comparative analysis of the above no-load characteristics and dynamic steady-state load conditions, the accuracy and precision of the nonlinear model considering saturation established by the magnetic saturation parameter identification method based on particle swarm optimization in this paper have been verified. At the same time, it has also been verified that in normal operation, saturation has a relatively small impact on sudden load loading and unloading.

5. Conclusions

This paper proposes a parameter identification method for magnetic saturation in hybrid excitation generators based on particle swarm optimization. By introducing a saturation correction coefficient into the flux linkage equation and identifying the parameters using PSO, a piecewise nonlinear representation of the stator and rotor inductance matrix is achieved, and a numerical simulation model capable of reflecting different saturation stages is established. Through comparison between simulation results and experimental data, the following conclusions are drawn:

1. The magnetic saturation effect significantly influences modeling accuracy. The proposed nonlinear fitting method effectively describes the flux linkage variation from the linear region to the saturation region.
2. The use of PSO for identifying magnetic saturation nonlinear parameters enables global optimization without requiring gradient information. The results show that this method achieves high identification accuracy and fast convergence. Quantitatively, the maximum relative error is reduced from 7.78% (of the original linear model) to 1.04%, corresponding to a reduction of approximately 86.6%. Meanwhile, the parameter identification time is drastically shortened: compared with the conventional 3D finite-element-based extraction, which typically takes several days, the PSO-based identification converges in about 5 h. These figures confirm the significant computational efficiency gain without compromising accuracy.
3. The proposed method overcomes the large errors of traditional linear models under saturation effects and provides a new approach for refined modeling and parameter identification of hybrid excitation generators.

Author Contributions: Conceptualization, R.J. and X.Y.; Methodology, R.J.; Software, R.J. and W.Y.; Validation, R.J.; Formal Analysis, R.J.; Investigation, R.J. and W.Y.; Resources, X.Y. and Y.J.; Data Curation, R.J.; Writing—Original Draft Preparation, R.J.; Writing—Review and Editing, R.J., X.Y., Y.J., Z.Y. and W.Y.; Visualization, R.J.; Supervision, X.Y., Y.J. and Z.Y.; Project Administration, R.J. and X.Y.; Funding Acquisition, X.Y. and Z.Y. All authors have read and agreed to the published version of the manuscript.

Funding: This research was funded by the National Natural Science Foundation of China, grant number 52107136 and the Natural Science Foundation of Hubei Province, grant number 2022CFB506. The APC was funded by the authors.

Data Availability Statement: The original contributions presented in the study are included in the article; further inquiries can be directed to the corresponding author.

Conflicts of Interest: The authors declare no conflicts of interest.

Abbreviations

The following abbreviations are used in this manuscript:

AM	Analytical method
AVR	Automatic Voltage Regulator
DFIG	Doubly fed induction generator
DSLPSO	Dynamic self-learning particle swarm optimization
EMN	Equivalent magnetic network
FEA	Finite element analysis

HEG	Hybrid excitation generator
ICPSO	Improved chaotic particle swarm optimization
IM	Induction motor
MEC	Magnetic equivalent circuit
NCPSO	Niche chaotic particle swarm optimization
PMSM	Permanent magnet synchronous motor
PSO	Particle swarm optimization
SPMSM	Surface-mounted permanent magnet synchronous motor
UR	Uncontrolled Rectification

References

1. Zhang, Z.R.; Wang, D.; Hua, W. Overview of Configuration, Design and Control Technology of Hybrid Excitation Machines. *Proc. CSEE* **2020**, *40*, 7834–7850+8221. [CrossRef]
2. Mbayed, R.; Salloum, G.; Monmasson, E.; Gabsi, M. Hybrid excitation synchronous machine finite simulation model based on experimental measurements. *IET Electr. Power Appl.* **2016**, *10*, 304–310. [CrossRef]
3. Zhang, Y.H.; Wu, X.Z.; Zheng, X.Q.; Lin, N. Field-circuit coupling simulation analysis of diode fault of 12-phaserectifier generators system. *Adv. Technol. Electr. Eng. Energy* **2019**, *39*, 71–78. [CrossRef]
4. Wang, Y.Z.; Wang, H.Z.; Liu, W.F.; Niu, X.Z.; Yang, C. A Novel Modeling Method for Power Generator Systems of Wound-excited Doubly Salient Machines. *Proc. CSEE* **2017**, *37*, 5162–5170+5236. [CrossRef]
5. Sergeant, P.; Bossche, A.V.D. Influence of the Amount of Permanent-Magnet Material in Fractional-Slot Permanent-Magnet Synchronous Machines. *IEEE Trans. Ind. Electron.* **2014**, *61*, 4979–4989. [CrossRef]
6. Asfirane, S.; Hlioui, S.Z.; Amara, Y.Q.; Gabsi, M. Study of a Hybrid Excitation Synchronous Machine: Modeling and Experimental Validation. *Math. Comput. Appl.* **2019**, *24*, 34. [CrossRef]
7. Jiang, S.X.; Peng, B. Development of Universal 3D Equivalent Magnetic Network Model for Yokeless and Segmented Armature Axial Flux Permanent Magnet Motor Using Edge Step Equivalent Method. *Trans. China Electrotech. Soc.* **2026**, *41*, 416–425+474. [CrossRef]
8. Tong, W.M.; Wang, P.; Wu, S.N.; Jia, J.G. Electromagnetic Performance Analysis of a Hybrid Excitation Synchronous Machine Based on 3D Equivalent Magnetic Network. *Trans. China Electrotech. Soc.* **2023**, *38*, 692–702. [CrossRef]
9. Sun, L.; Sun, Z.H.; Feng, S.S.; Zhang, Z.R. Nonlinear Magnetic Network Analysis of a Novel Hybrid Excitation Doubly Salient Machine. *Small Spec. Electr. Mach.* **2015**, *43*, 21–26.
10. Xu, W.; Zhang, Y.S.; Cao, C.; Huang, S.D.; Gao, J.; Wang, X.; Gao, Y.Z.; Gao, X.H. Improved Construction Method of Nonlinear Varying Equivalent Magnetic Network Model for Hybrid Excitation Asymmetric Stator Pole Double Salient Machine. *Proc. CSEE* **2023**, *43*, 304–318. [CrossRef]
11. Guo, K.Y.; Li, Y.H.; Shi, L.M.; Zhou, S.J.; Xu, F. Non-Linear Mathematic Model of a Segmented Powered Permanent Magnet Linear Synchronous Machine. *Trans. China Electrotech. Soc.* **2021**, *36*, 1126–1137. [CrossRef]
12. Sergeant, P.; Vansompel, H.; Hemeida, A.; Bossche, A.V.D.; Dupré, L. A Computationally Efficient Method to Determine Iron and Magnet Losses in VSI-PWM Fed Axial Flux Permanent Magnet Synchronous Machines. *IEEE Trans. Magn.* **2014**, *50*, 8101710. [CrossRef]
13. Zhang, Z.R.; Sun, L.; Tao, Y.Y.; Yan, Y.G. Development of nonlinear magnetic network model of a hybrid excitation doubly salient machine. In Proceedings of the 2013 International Electric Machines & Drives Conference, Chicago, IL, USA, 12–15 May 2013.
14. AlRashidi, M.R.; El-Hawary, M.E. A Survey of Particle Swarm Optimization Applications in Electric Power Systems. *IEEE Trans. Evol. Comput.* **2009**, *13*, 913–918. [CrossRef]
15. del Valle, Y.; Venayagamoorthy, G.K.; Mohagheghi, S.; Hernandez, J.-C.; Harley, R.G. Particle Swarm Optimization: Basic Concepts, Variants and Applications in Power Systems. *IEEE Trans. Evol. Comput.* **2008**, *12*, 171–195. [CrossRef]
16. Shami, T.M.; El-Saleh, A.A.; Alswaitti, M.; Al-Tashi, Q.M.; Summakieh, A.; Mirjalili, S. Particle Swarm Optimization: A Comprehensive Survey. *IEEE Access* **2022**, *10*, 10031–10061. [CrossRef]
17. Liu, Z.H.; Wei, H.L.; Li, X.H.; Liu, K.; Zhong, Q.C. Global Identification of Electrical and Mechanical Parameters in PMSM Drive Based on Dynamic Self-Learning PSO. *IEEE Trans. Power Electron.* **2018**, *33*, 10858–10871. [CrossRef]
18. Kolsi, H.; Benhadj, N.; Guesmi, T.; Marouani, I.; Alshammari, B.M.; Alsaif, H.; Alqunun, K.; Neji, R. Optimal Design of a PMSM for Electric Vehicle Using Chaotic Particle Swarm Optimizationv. *IEEE Access* **2024**, *12*, 170273–170294. [CrossRef]
19. Li, J.; Yang, S.Y.; Xie, Z.; Zhang, X. Online Parameter Identification of Permanent Magnet Synchronous Motor Based on Fast Particle Swarm Optimization Algorithm with Effective Information Iterated. *Trans. China Electrotech. Soc.* **2022**, *37*, 4604–4613.
20. Li, J.; Yang, S.Y.; Xie, Z.; Zhang, X. Parameter Identification of PMSM Based on improved chaos PSO algorithm. *Transducer Microsyst. Technol.* **2023**, *42*, 157–160.

21. Xie, C.; Zhang, S.; Li, X.; Zhou, Y.; Dong, Y. Parameter Identification for SPMSM with Deadbeat Predictive Current Control Using Online PSO. *IEEE Trans. Transp. Electrif.* **2024**, *10*, 4055–4064. [CrossRef]
22. Liu, X.P.; Hu, W.P.; Ding, W.Z.; Xu, H.; Zhang, Y. Multi-parameter identification of permanent magnet synchronous motor based on improved particle swarm optimization. *Trans. China Electrotech. Soc.* **2020**, *35*, 1198–1207. [CrossRef]
23. Chen, G.Y.; Guo, W.; Huang, K.S. On Line Parameter Identification of an Induction Motor Using Improved Particle Swarm Optimization. In Proceedings of the 2007 Chinese Control Conference, Zhangjiajie, China, 26–31 July 2007.
24. Xiang, X.C.; Diao, R.S.; Bernadin, S.; Foo, S.Y.; Sun, F.Y.; Ogundana, A.S. An Intelligent Parameter Identification Method of DFIG Systems Using Hybrid Particle Swarm Optimization and Reinforcement Learning. *IEEE Access* **2024**, *12*, 44080–44090. [CrossRef]
25. Su, W.; Lin, N.; Zhang, X.B.; Wang, D.; Guo, Y.J.; Wei, K. Research on Mathematical Model of a Consequent-pole Hybrid Excitation Synchronous Generator. *Proc. CSEE* **2023**, *43*, 1569–1579.
26. Detka, K.; Górecki, K. Electrothermal Model of Coupled Inductors with Nanocrystalline Cores. *Energies* **2022**, *15*, 224. [CrossRef]
27. Valchev, V.; Bossche, A.V.D. Eddy current losses and inductance of gapped foil inductors. In Proceedings of the IEEE 2002 28th Annual Conference of the Industrial Electronics Society, Seville, Spain, 5–8 November 2002.
28. Tumanski, S.; Bakon, T. Measuring System for two-Dimensional Testing of Electrical Steel. *J. Magn. Magn. Mater.* **2001**, *223*, 315–325. [CrossRef]
29. Kennedy, J.; Eberhart, R.C. Particle swarm optimization. In Proceedings of the ICNN'95—International Conference on Neural Networks, Perth, WA, Australia, 27 November–1 December 1995; pp. 1942–1948.
30. He, H.Y.; Sheng, Y.F. Photovoltaic Expansion Perception Method Based on GWO-PSO-Optimized Robust Extreme Learning Machine. *Energies* **2026**, *19*, 2350. [CrossRef]